fluids

MDPI

Article

Research on the Flow Mechanism of a Large-Scale Wind Turbine Blade Based on Trailing Edge Flaps

Yifan Liu [1], Mingming Zhang [1,*], Bingfu Zhang [1], Haikun Jia [2], Na Zhao [2] and Zhaohuan Zhang [3]

[1] Institute of Green-Low Carbon Energy Innovative Technology, Harbin Institute of Technology (Shenzhen), Shenzhen 518055, China; 17851981718@163.com (Y.L.); zhangbfu@hit.edu.cn (B.Z.)
[2] National Key Laboratory of Renewable Energy Grid-Integration, China Electric Power Research Institute, Beijing 100192, China; jiahaikun@epris.gcc.com.cn (H.J.); zhaona@epri.sgcc.com.cn (N.Z.)
[3] Economic & Technology Research Institute, State Grid Shandong Electric Power Company, Jinan 250021, China; zhangzhaohuan0536@163.com
* Correspondence: mmzhang@hit.edu.cn

Abstract: This study was performed based on the previous work of this research group to promote the practical engineering application of trailing edge flaps. Specifically, the established "intelligent blade" simulation platform was used for simulation calculations, bringing about the achievement of a significant load reduction effect in which the standard deviation of the blade root pitching moment decreased by 12.4% under the influence of the trailing edge flap. Then, the dynamic conditions of the wind turbine and trailing edge flap under active control, obtained from the "intelligent blade" simulation platform, were input into CFD for further high-fidelity simulations. Additionally, a simulation method that allows for the real-time observation of the flow field was optimized with CFD as a flow field visualizer. This approach assisted in analyzing how the trailing edge flap affects the flow characteristics around the blade. The results reveal that the deflection of the trailing edge flap generated new vortex structures. These new vortex structures interacted with the pre-existing vortex structures. Moreover, the vortex structures produced by flap deflection supplemented the energy dissipation caused by flow separation on the leeward surface of the blade, contributing to the weakening of flow separation on the leeward side of the blade, affecting the pressure exerted by the fluid on the blade surface, and ultimately lowering the blade's load.

Keywords: DTEF; CFD; flow mechanism

check for updates

Academic Editor: Mahmoud Mamou

Received: 3 April 2025
Revised: 20 May 2025
Accepted: 2 June 2025
Published: 14 June 2025

Citation: Liu, Y.; Zhang, M.; Zhang, B.; Jia, H.; Zhao, N.; Zhang, Z. Research on the Flow Mechanism of a Large-Scale Wind Turbine Blade Based on Trailing Edge Flaps. *Fluids* **2025**, *10*, 157. https://doi.org/10.3390/fluids10060157

Copyright: © 2025 by the authors. Licensee MDPI, Basel, Switzerland. This article is an open access article distributed under the terms and conditions of the Creative Commons Attribution (CC BY) license (https://creativecommons.org/licenses/by/4.0/).

1. Introduction

With the development of the wind power industry, the scaling up of wind turbines is an inevitable path to reducing the levelized cost of electricity (LCOE). However, the overall load on the wind turbine system substantially increases with the growing capacity of wind turbines and blade sizes. This higher load brings about the diminished reliability of the wind turbine system and increases costs in manufacturing, production, and operational maintenance, becoming a major obstacle to reducing the LCOE and advancing lightweight blade development.

Inspired by the aileron of aircraft, the active control approach based on trailing edge flap (DTEF) deflection offers a more sensitive response to small amplitude load variations compared to independent pitch control [1]. It can effectively control the loads experienced by various components of the wind turbine system [2] and has thus attracted considerable attention. This active control technique can remarkably enhance the overall performance

and reliability of the wind turbine by lowering loads, improving system stability, and minimizing mechanical stresses, which are crucial for large-scale turbines operating in dynamic wind conditions [3]. Consequently, numerous studies have been conducted to explore its potential applications and optimize its design for practical use in wind energy systems.

The DTEF has significant potential for load control to optimize its performance. Extensive studies have been performed on the design of controllers for the DTEF to exploit its load control effectiveness. Among them, the Proportional–Integral–Derivative (PID) controller is widely applied because of its simple principle, ease of implementation, and broad applicability. However, many researchers have attempted to incorporate intelligent control algorithms, such as fuzzy control and neural network control, into the design of DTEF controllers for wind turbines with the rapid development of artificial intelligence (AI) technologies in recent years. Controllers such as single-neuron PID controllers and adaptive PID controllers have been developed, enabling DTEFs to satisfy the complex control demands of nonlinearity and strong disturbances under challenging conditions [4,5]. Concurrently, experimental studies have revealed that the root flap pitching moment and the load on the flap are the two most recognized sensor signals. These signals allow for faster and more efficient control compared to sensor signals such as tip displacement and tip pitching acceleration [6]. Meanwhile, Model Predictive Control (MPC), as a control method considering the system's dynamic characteristics and constraints, optimizes control by predicting future system states while providing robustness and good performance. Some researchers have adopted the MPC strategy to achieve optimal control of the flap position [7,8].

As the control effectiveness of the DTEF gains increasing recognition, simulation-based approaches have become the primary method to conduct in-depth studies on the DTEF owing to the limitations of external field experimental conditions. Thus, many researchers, such as Gaunaa's team from the Technical University of Denmark (DTU) and the team from the Delft University of Technology (TU Delft) [9], developed simulation models to better simulate the aerodynamic characteristics and flow field features of wind turbines with the DTEF. These include dynamic stall engineering models, fully resolved CFD models, and viscous–inviscid interaction-free wake vortex models. Among them, the fully resolved CFD model demonstrates the best simulation of the aerodynamic characteristics of the airfoil, while the other two engineering models have limitations in simulating dynamic stall conditions. However, these models still yield good simulation results under conventional conditions.

Multiple studies on the flow field characteristics of two-dimensional airfoils with the DTEF have been performed to address the control mechanism of the DTEF. A team from the University of Maryland [10], along with Wolff, Qian, and others, conducted high-fidelity simulations and experiments on two-dimensional airfoils with the DTEF. They reported that the best fatigue load control effect occurs when the DTEF changes in the opposite direction to the angle of attack of the airfoil, providing theoretical support for flap optimization design. Furthermore, Zhang M.M. [11–13] and Yang [14] investigated the load reduction of large wind turbine blades using the DTEF to fully consider the operational conditions of actual wind turbines and explore the load reduction mechanism of the DTEF. Additionally, the working mechanism of the flap was explained from the perspective of the phase relationship between blade aerodynamics and structural deformation. Specifically, the deflection of the DTEF accelerates the energy dissipation in the region near the flap, effectively weakening the normal force acting on the blade. This, in turn, affects aeroelastic coupling on the blade. The aerodynamic characteristics of the entire blade can be improved by controlling the oscillation of the DTEF.

Extensive studies have been performed on various aspects of the DTEF. The DTEF has already established a preliminary foundation for engineering practical application and development. The next critical step is to conduct an aerodynamic optimization design for the DTEF. This article provides theoretical support for the engineering application of trailing edge flaps by exploring the flow control mechanism of trailing edge flaps rather than directly designing trailing edge flaps. First, the "Smart Blade" simulation platform, based on the research team's previous work [11–14], was utilized to obtain the load reduction effect of the DTEF. Subsequently, the incoming flow information and flap motion data were input into CFD (Computational Fluid Dynamics). By leveraging CFD, a computational method capable of capturing real-time flow field characteristics, the flow field was employed as a display tool to explore the key factors affecting the load in the flow field. Our research group investigated how the DTEF reduces the overall blade load and explored the load reduction mechanism, providing theoretical support for the practical application of the DTEF and the subsequent optimization design of controllers.

2. Methodology

2.1. Intelligent Blade Simulation Platform

In this study, the load reduction effect of the DTEF under active control was first obtained by the "Smart Blade" simulation platform to investigate how the DTEF under active control conditions affects the flow field and consequently reduces the blade load. The simulation platform was developed by integrating a trailing-edge flap controller into the baseline NREL 5MW wind turbine controller within OpenFAST—an efficient open-source simulation tool for wind turbines, and the principle of operation of this platform is shown in Figure 1. This enhanced platform not only maintains the capability to simulate normal turbine operations but also achieves blade load reduction through active trailing-edge flap deflection control. The validity of the simulation results obtained from this OpenFAST-based platform has been extensively verified in a series of publications by Professor M.M Zhang's research team [11–14].

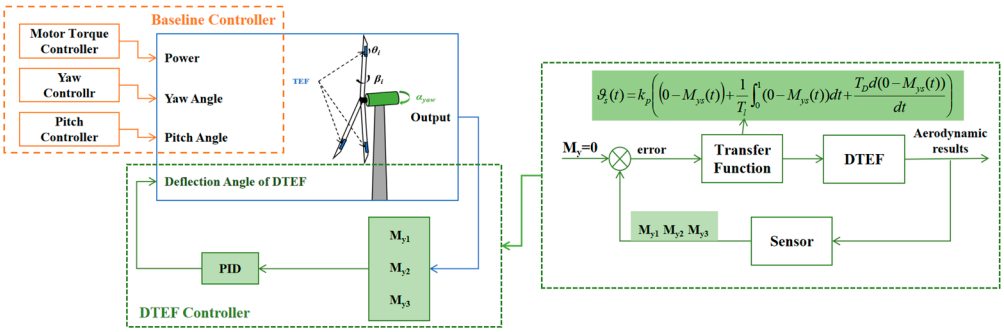

Figure 1. Schematic diagram of flap control platform.

The main control system for the wind turbine used the baseline controller system provided for the NREL 5 MW reference wind turbine. The DTEF control system was completely independent of the main control system of the wind turbine. With a classic PID controller, it reduced the fluctuation in the measured root bending moment (M_{y1}) on the turbine blade by adjusting the deflection angle of the DTEF. This control approach was employed to achieve closed-loop control of the blade load.

Through an inverse Kalman transformation, the platform transformed the aerodynamic calculations of the root bending moment from the rotating coordinate system to the fixed coordinate system. In the fixed coordinate system, the flap deflection angle was obtained through the control equation, and then the flap deflection angle was converted

from the fixed coordinate system back to the rotating coordinate system to control flap deflection through the Kalman transformation.

Following the PID control law with the aim of minimizing the root bending moment, the reference value was set to 0. By incorporating the data, the motion control equation for the DTEF was obtained as follows:

$$\vartheta_s(t) = k_p\left((0 - M_{ys}(t)) + \frac{1}{T_l}\int_0^1 (0 - M_{ys}(t))dt + \frac{T_D d(0 - M_{ys}(t))}{dt}\right) \quad (1)$$

where k_p represents the proportional coefficient, T_l denotes the integral time constant, and T_D embodies the differential time constant.

During the design process of the DTEF controller, the gains were selected to significantly curtail the fluctuations in the root bending moment while maintaining the power output. After repeated trials, the control parameters were determined, with T_l set to 2, T_D set to 0.02, and k_p set to 0.054.

2.2. Computational Fluid Dynamics Simulation

As exhibited in Figure 2, the NREL 5 MW wind turbine rotor geometry model was established with the geometric data provided in the official documentation of the NREL 5 MW wind turbine. The key parameters of the NREL 5MW wind turbine are shown in Table 1. Based on the hub dimensions specified in the official documentation, a cylinder with the same size was employed to simulate the rotor hub. Additionally, the trailing edge flap was positioned along the blade span between 60% and 80%, covering 10% of the chord length. During the CFD simulation, the trailing edge flap was modeled separately from the blade body to avoid negative volume issues arising from the deflection of the flap. In the simulation, the trailing edge flap was treated as a rigid flap for deflection control.

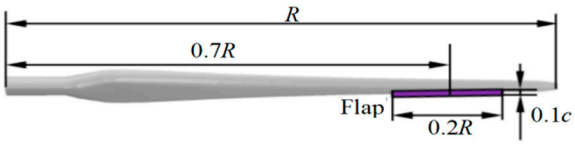

Figure 2. Blade geometric model.

Table 1. Key parameters of NREL 5MW wind turbine.

Name	Number	Unit
Rated Power	5000	kW
Rated Speed	11.4	m/s
Rotor Diameter	126	m
Hub Height	90	m

Considering the rotor's rotation, the entire flow field was divided into two parts: the rotating region of the rotor and the stationary region.

The stationary flow field part was modeled as a square flow domain to satisfy the wind shear velocity inlet condition. The outer domain width was set to 3*D* (where *D* indicates the rotor diameter) to avoid the impact of velocity gradients at the boundary walls of the square flow field on the rotor flow field. The rotor center was placed 90 m above the ground to align with the hub height of the NREL 5 MW wind turbine. Specifically, the upper wall was positioned at a distance of 3*D* from the rotor center; the inflow surface was placed at a distance of 2*D* from the rotor; and the outlet wall was placed at a distance of 10*D* from the rotor center, and those make up the flow field around the impeller, as depicted in Figure 3.

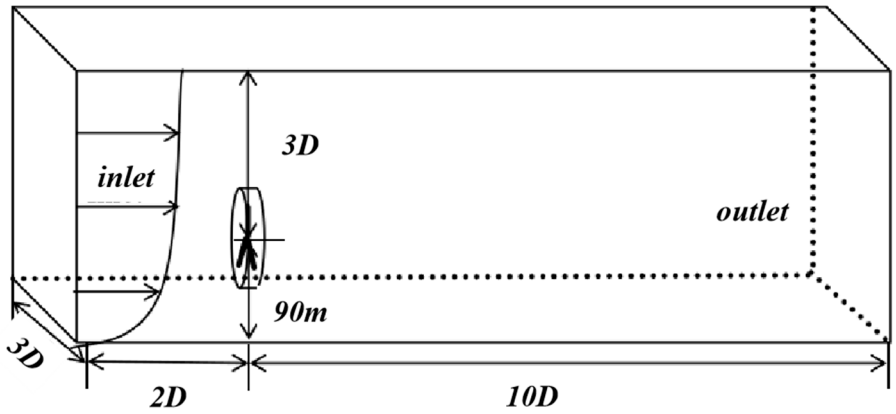

Figure 3. Flow field diagram.

The shape and structure of the wind turbine are relatively complex, and the chord length varies significantly from the root to the tip of the blade. With the purpose of minimizing the computational resources while meeting the required number of nodes, the blade along its span was divided into three parts: the root (0~60%), the mid-span (60~80%), and the tip (80~100%). Different mesh sizes were applied to each section for grid generation. In the grid independence study, four different mesh densities were compared, with a design wind speed of 11.4 m/s as the reference state. The grid parameters and corresponding torque calculation results for the wind turbine are listed in Table 2.

Table 2. Grid independence verification.

	Grid Quantity (Million)	Torque (Nm)	Error (%)
G1	17.49	3.70×10^6	8.7838
G2	18.59	4.03×10^6	1.0186
G3	20.54	4.07×10^6	0.5903
G4	21.14	4.09×10^6	/

As observed from Table 2, the rate of change in the blade torque was only 1.02% when the number of grids reached 18.59 million. The grid size at this point met the simulation calculation requirements. Thus, a grid size corresponding to 18.59 million grids was selected for subsequent grid generation and simulation calculations to save computational costs and reduce time consumption. And the details of the mesh are shown in Table 3.

Table 3. Details of mesh.

Region	0–0.6r/R of Blade	0.6–0.8 r/R of Blade	0.8–1 r/R of Blade	Flow Field
Unit size	5 m	2 m	1 m	10 m
Thickness of first layer of mesh	0.5 mm	0.4 mm	0.2 mm	/
Number of layers of boundary layer mesh	8	8	8	/
Expansion rate	1.15	1.15	1.15	/

Numerical simulation calculations were performed using the commercial software Ansys Fluent 2024R2. The turbulence model used as the Standard k-ω model, which performed well in simulating wall boundary layers, free shear flows, and high Reynolds number flow characteristics. It is suitable for boundary layer flow and separation as well as transition under adverse pressure gradients. In addition, the Unsteady Reynolds-Averaged Navier–Stokes (URANS) equations were solved. A sliding mesh was utilized for

information exchange between the rotor-rotating domain and the stationary flow domain. The discretization solution was conducted using a second-order Euler equation-based dual-time stepping implicit integration algorithm. Table 4 lists the details of the Fluent simulation calculation.

Table 4. Numerical calculation method conditions.

Name	Setting
Method	URANS
Model	Standard k-ω
U_{inlet}	11.4 m/s
Rotor Speed	12.1 rpm
Time step	0.005

Under the above conditions, model validity verification was conducted by comparing the results with the thrust and torque data provided in the official IEA [15] documentation. As revealed in Figure 4, the simulated thrust and torque were 714.55 kN and 4138.94 kNm, respectively. The deviations from the design data for thrust and torque were 5.71% and 7.43%, respectively, which are within a reasonable error range.

$$P = T\omega = \frac{Tn}{9.55 \times 10^6} \tag{2}$$

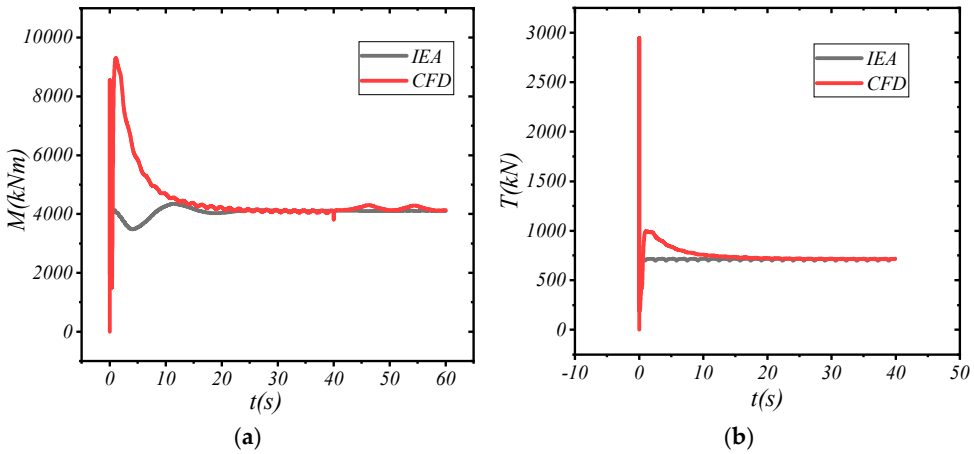

Figure 4. The model's validity is verified as follows: (**a**) impeller torque; (**b**) impeller thrust.

The torque was converted into the generated power for comparison to further assess whether the CFD conditions were correctly set. Using Equation (2), the generated power was calculated to be 5.24 MW. Compared to the NREL 5 MW rated power, the calculation result deviated by only 4.88%. This level of error indicates that the accuracy of the CFD conditions is reasonable and effectively reflects the actual performance of the system.

3. Analysis of Simulation Results

3.1. Simulation Results of OpenFAST

3.1.1. Boundary Condition Setting

The incoming wind conditions considered in the OpenFAST and CFD simulations are vertical wind shear inflow. Concerning the aerodynamic performance simulation and the

load calculation of standard wind turbines, the wind turbine design specifications require that the normal wind profile follows the power law formula,

$$V_{inlet} = V_{\infty} \times (h/H)^{\alpha} \quad (3)$$

where the wind speed profile exponent α is set to 0.2.

The height above the ground and the wind speed were used as the horizontal axis and the vertical axis, respectively, to verify the accuracy of the inlet boundary condition calculation. During the OpenFAST and CFD simulations, characteristic points on the inlet plane (as shown in Figure 3, the wind is input from the left side and output from the right, so the left side is defined as the inlet plane) were defined, and velocity monitors were set at these points to record the simulation data. The results are illustrated in Figure 5; as we can see, at the hub height (90 m), the incoming flow velocity corresponds to the rated wind speed of 11.4 m/s. According to the wind shear profile, the inflow velocity decreases below 11.4 m/s at altitudes lower than 90 m, while it exceeds 11.4 m/s at positions above 90 m.

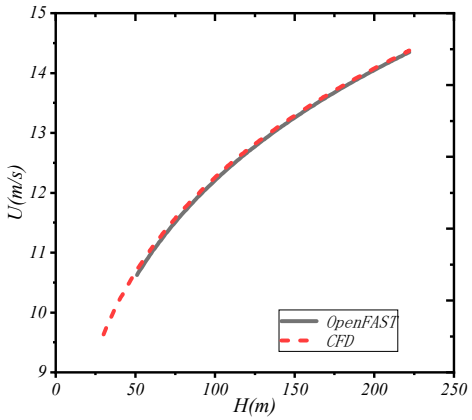

Figure 5. Distribution of wind speed with height.

3.1.2. OpenFAST Simulation Results

The operation of the wind turbine under 12 m/s inflow conditions was simulated on the OpenFAST simulation platform. Figure 6 displays the time-domain signal results for a randomly selected period within 20 rotor rotations with Blade 1 as an example.

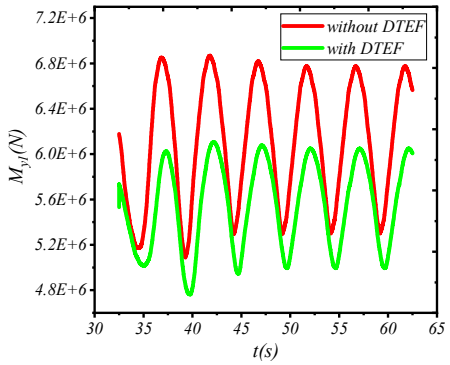

Figure 6. The effect of the blade root flapwise moment with the deflection of the DTEF.

As suggested in Figure 6, the root flap bending moment was effectively controlled, with the mean and standard deviation being reduced by 20.58% and 13.2%, respectively.

As shown in Figure 7, it can be seen from the variation in the deflection angle of the trailing edge flap with time that the deflection and load changes in the trailing flap show

a periodic change trend. At the same time, we fit the curve of the trailing flap angle with time as a function of time and write a UDF as a CFD boundary condition and input Fluent.

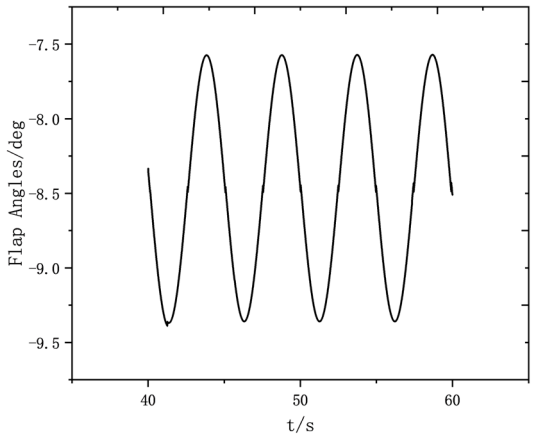

Figure 7. The deflection angle of the Blade 1 flap changes over time.

3.2. CFD Simulation Results

Under the same boundary conditions, the blade and DTEF dynamics obtained from the OpenFAST simulations can be expressed as a time-dependent equation and implemented into CFD simulations through user-defined functions (UDFs), enabling the dynamic conditions to be recognized by the CFD solver for subsequent numerical simulations. A total of twenty rotor rotations were simulated, and the computational data from the final few converged cycles were analyzed.

Figure 8 presents the numerical simulation results of the thrust variations with and without the DTEF. After flap deflection, the average thrust on Blade 1 and the standard deviation decreased by 20.03% and 13.82%, respectively, showing good agreement with the results obtained from the OpenFAST simulation. This confirms that the DTEF exerted a noticeable effect in reducing the blade load.

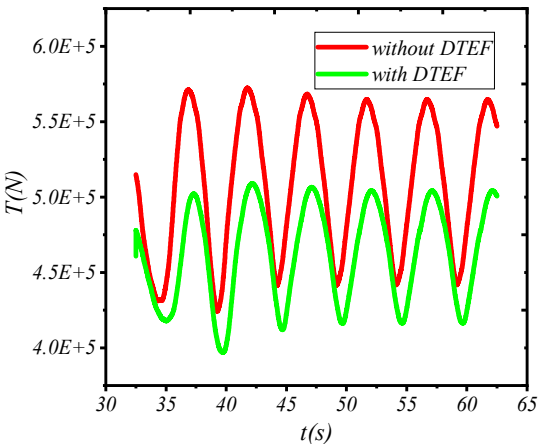

Figure 8. The temporal curve of the thrust on Blade 1 with the action of DTEF deflection.

The tangential force coefficient and normal force coefficient along the blade spanwise position at four typical azimuth angles throughout the entire rotation cycle were extracted to obtain a better understanding of the variation in the blade aerodynamic characteristics

before and after the deployment of the flap. The calculation of tangential and normal force coefficients can be expressed as

$$C_N(y) = \frac{F_N}{\rho[W^2 + (y\Omega)^2]c(y)/2} \tag{4}$$

$$C_T(y) = \frac{F_T}{\rho[W^2 + (y\Omega)^2]c(y)/2} \tag{5}$$

where W denotes the incoming wind speed, y represents the distance from the calculation point to the center of rotation, Ω refers to the rotor rotational angular velocity, and c indicates the local chord length.

In this study, we define θ in Figure 9 as the azimuth angle of the blade, and θ is equal to 0° when the blade is perpendicular to the ground upward.

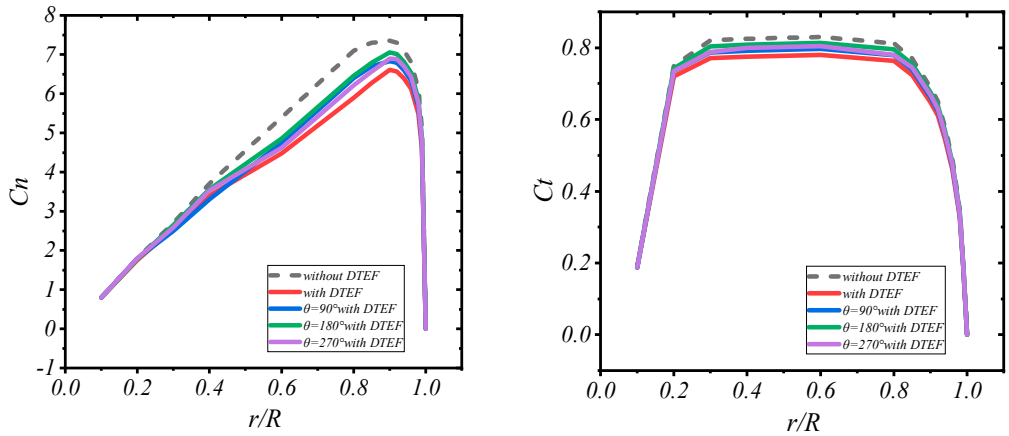

(**a**) (**b**)

Figure 9. The force coefficient distribution along the longitudinal direction of Blade 1. (**a**) Normal force coefficient. (**b**) Tangential force coefficient.

As demonstrated in Figure 9, the deflection of the flap affected the overall aerodynamic characteristics of the blade spanwise, with the most significant impact occurring near the region where the flap was located ($0.4 < r/R < 0.9$).

The farther from the flap, the smaller the effect. In the region where the flap presented the most influence, the normal force coefficient of the airfoil decreased by approximately 15%, and the tangential force coefficient dropped by about 2%. In other words, while the deflection of the DTEF sacrificed a small amount of power generation, it resulted in a significant reduction in the blade load.

The distribution of the normal force coefficient and tangential force coefficient along the blade spanwise at four typical azimuth angles (θ in Figure 9) implies that the deflection of the flap affected the normal and tangential force coefficients at different blade section positions for different azimuth angles. This difference was induced by the varying deflection of the DTEF at different azimuth positions. Furthermore, the degree of influence of the DTEF on the normal and tangential force coefficients at different azimuth positions followed the same trend as the load experienced by the blade at those positions. Specifically, taking the 0° azimuth position as an example, when the blade is vertically oriented upward at this position, it experiences higher mean wind speeds and consequently bears the maximum load. At this critical orientation, the trailing-edge flap demonstrates its most pronounced load reduction effect. Correspondingly, the tangential force coefficient and normal force coefficient on the blade surface at 0° azimuth show the most significant

variations compared to the baseline blade. This is one of the reasons why the DTEF can effectively reduce the amplitude of blade load fluctuations.

4. Flow Mechanism Analysis

An in-depth study of the flow characteristics near the wall was conducted to comprehend the flow physics of how the DTEF affects the aerodynamic properties of the blade. The flow field around the blade only exhibited differences in velocity magnitude throughout the entire rotational cycle and thus similar flow patterns across the entire cycle. Thus, a detailed analysis could be performed with a blade azimuth angle of 0° as a typical case. At this azimuth angle, the flow characteristics effectively demonstrated aerodynamic behavior throughout the entire rotational cycle. In addition, the deflection of the DTEF affected the aerodynamic characteristics of the entire blade from the 40% to 90% spanwise position. To reveal the underlying mechanism by which the DTEF influenced the aerodynamic performance of the blade, this section focuses on studying the flow characteristics near the wall, such as boundary layer separation and the corresponding flow structures.

As mentioned earlier, the flexible DTEF alters the thrust experienced by the blade. According to classical BEM (Blade Element Momentum) theory, the axial thrust T on any infinitesimal segment of a single blade is expressed as

$$dT = \frac{\rho V_{total}^2 c}{2}(C_L \cos\delta + C_D \sin\delta)dr \tag{6}$$

where ρ denotes the density of the incoming airflow; c represents the chord length; V_{total} indicates the relative inflow velocity to the blade; C_L embodies the lift coefficient; C_D refers to the drag coefficient; δ stands for the angle of attack, which is the sum of the pitch angle β and the aerodynamic angle of attack α; and T describes the axial thrust on the blade.

Yang [12] analyzed the key factors affecting blade thrust around the DTEF, revealing that the lift coefficient at most positions of the NREL 5 MW wind turbine blade is primarily influenced by the magnitude of the normal force coefficient. The relationship between the normal force coefficient and the pressure coefficient [16] can be expressed as

$$C_l = \frac{1}{x_{te} - x_{le}} \int_{x_{le}}^{x_{te}} (C_{pl}(x) - C_{pu}(x))dx \cdot \cos\alpha \tag{7}$$

where α stands for the angle between an airfoil's chord line and the horizontal reference line.

The above formula specifies that the magnitude of the unit airfoil's normal force coefficient is equal to the area enclosed by the pressure coefficient on the surface of the airfoil. This reflects that the thrust experienced by the blade before and after the DTEF is directly influenced by the surface pressure of the blade.

Figure 10 shows the characteristic blade cross-sectional locations, and Figure 11 illustrates the pressure coefficient curve at a typical section position, where the pressure coefficient is calculated as

$$-c_p = -\frac{(P - P_0)}{1/2 \times \rho \times V^2} \tag{8}$$

where P denotes the absolute pressure, P_0 embodies the atmospheric pressure at infinity from the rotor, ρ represents the air density, and V indicates the sectional velocity.

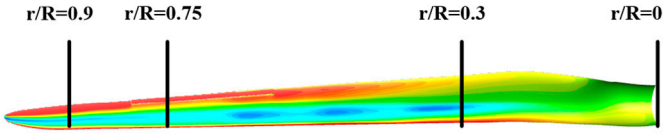

Figure 10. Schematic diagram of characteristic blade cross-sectional locations.

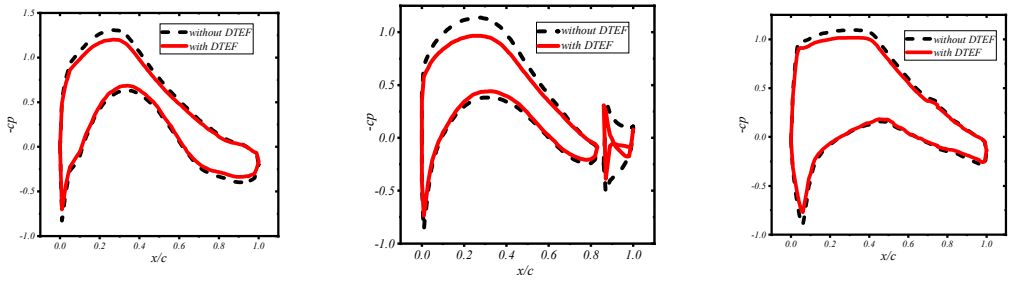

(**a**) r/R = 0.3 (**b**) r/R = 0.75 (**c**) r/R = 0.9

Figure 11. Blade section pressure coefficient curve.

The pressure coefficient at different cross-sections of the blade was affected by the DTEF. Among them, the pressure coefficient at the blade's midsection was most notably impacted, with the area enclosed by the pressure coefficient decreasing by 15%. Upon the relationship between the normal force coefficient and the pressure coefficient, as expressed in Equation (7), the deflection of the DTEF effectively adjusted the pressure distribution around the blade, contributing to lowering the normal force coefficient of the blade's cross-section. This suggests a decrease in the load on the blade.

Meanwhile, the pressure coefficient curve of the blade's cross-section (Figure 10) implies that the deflection of the DTEF lessened not only the pressure difference between the upper and lower surfaces of the airfoil but also the absolute value of the pressure acting on the blade surface. The aeroelastic coupling effect indicates that the force exerted by the air on the blade was reduced, and thus, the aeroelastic interaction between the blade and the surrounding air was weakened, bringing about the further improved aerodynamic performance of the blade during operation.

The impact of the flap can be observed from the blade surface pressure distribution contour map. Figure 12 displays the pressure distribution contour map on the blade's surface. Figure 13 shows the pressure distribution contour map at a typical cross-sectional location in the flow field. As demonstrated in the pressure contour map, for the baseline blade, a pressure concentration phenomenon appeared at the trailing edge of the windward surface at the 30% span location under the operating conditions of the wind turbine due to flow obstruction. It developed toward the leading edge of the blade tip. Simultaneously, a local negative pressure concentration region emerged near the 30–65% span range on the windward surface. On the suction side, a negative pressure region induced by flow separation extended from the 20% span leading edge position to the blade tip.

After the deflection of the DTEF, the pressure concentration phenomenon at the trailing edge of the windward surface was significantly weakened. Meanwhile, the negative pressure region on the suction side was reduced, especially in the position where the flap was located, and the suction side exhibited positive pressure. The overall change in the pressure distribution on the blade surface is consistent with the change in the pressure coefficient curve at the typical cross-sectional location shown earlier.

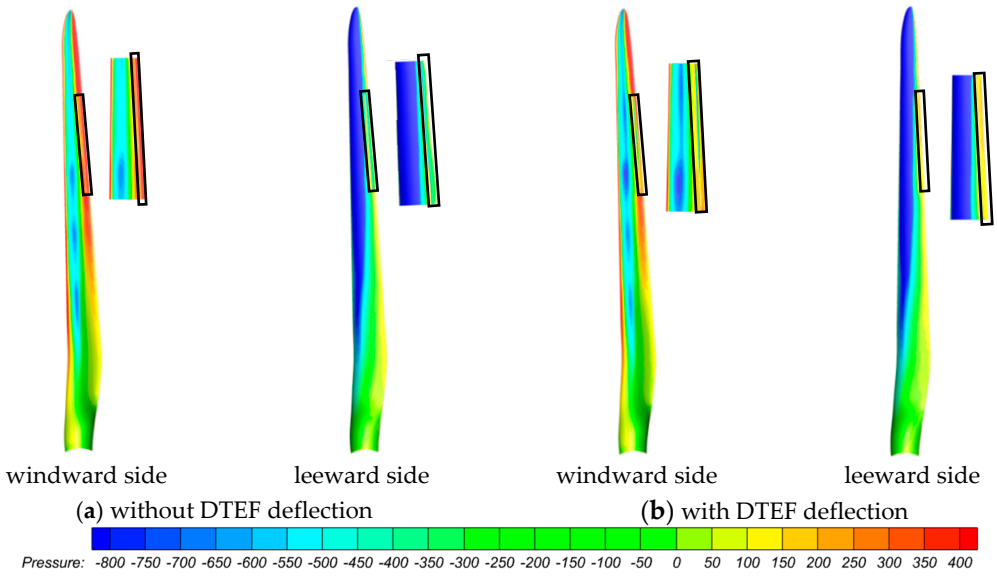

Figure 12. Pressure (Pa) distribution contour map on blade surface.

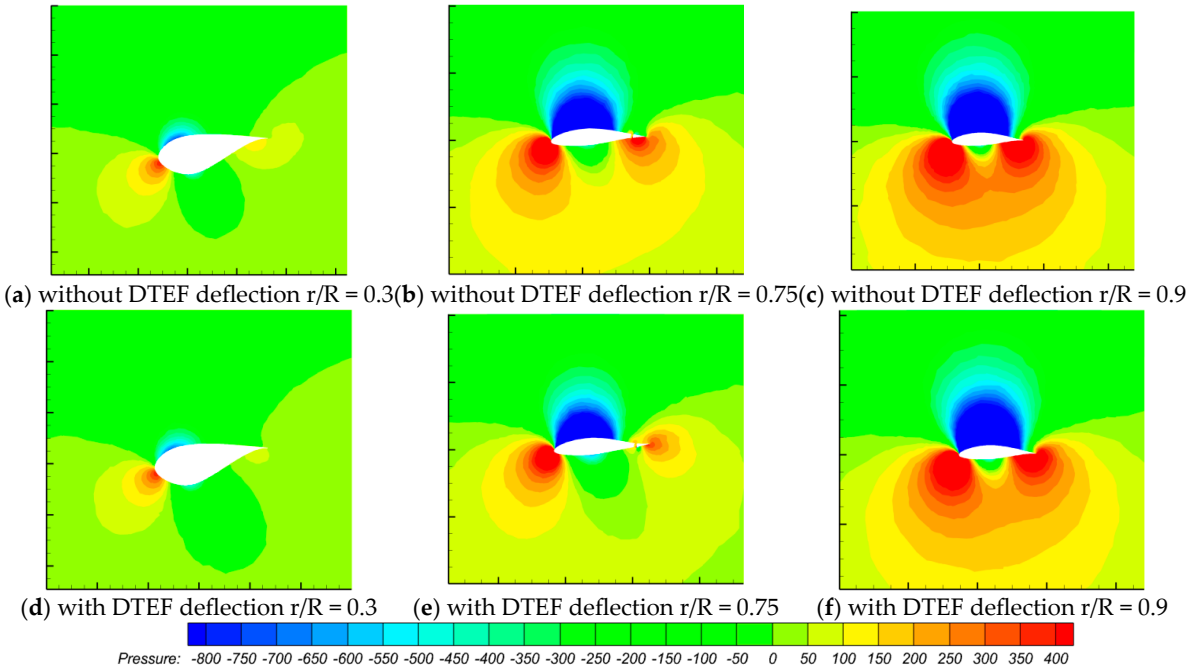

Figure 13. The pressure distribution of the flow field at a typical section of the blade.

The pressure distribution contour map in the flow field at the typical cross-sectional location (Figure 13) shows that for the baseline blade, high-pressure concentration regions appeared at both the trailing edge and leading edge of the blade, attributed to the obstruction of fluid flow by the blade. The closer to the blade tip, the larger the high-pressure area. Concurrently, the incoming air was subjected to significant flow diversion at the middle position of the windward surface of the airfoil owing to the special shape of the airfoil, leading to a local negative pressure at the middle of the windward surface of the airfoil.

Some descriptions of the flow field of the baseline and controlled cases should be provided first, followed by the comparisons. The deflection of the DTEF curtailed the blade's obstruction to the fluid at the trailing edge and hence the high-pressure concentration region at the trailing edge. Meanwhile, the deflection of the DTEF enhanced the disturbance in the flow field at the location of the flap, promoting the mixing of the fluid between the windward and suction sides of the blade. Consequently, local positive pressure

emerged around the trailing edge of the suction side at the flap's location. Additionally, the pressure difference between the windward and suction sides of the blade decreased, implying the lowered thrust on the blade.

According to Bernoulli's principle, there is a direct relationship between the velocity field and the pressure field. In the velocity field, the shape and distribution of the streamlines directly influence the pressure distribution. Therefore, the velocity streamline distribution contour map at the same cross-sectional location as the one above was extracted in this study.

As the comparison of the velocity streamline contour maps before and after the deflection of the DTEF (Figure 14) specifies, the zero-velocity point on the blade surface shifted towards the trailing edge of the airfoil after the deflection of the DTEF. In this study, the flow separation point is defined as the position where the flow velocity is zero. Therefore, velocity streamline contour maps at several typical spanwise cross-sectional locations on the blade were extracted. The effect of delayed flow separation was more noticeable in the region near the root of the blade, where flow separation was more severe. The delayed flow separation reduced the vortex and separated regions in the airflow, which in turn improved the pressure distribution on the blade surface. This suppressed the low-pressure regions provoked by flow separation. Simultaneously, the deflection of the flap enhanced the mixing of fluid between the windward and suction sides of the blade at the trailing edge, lessening the pressure difference between the windward and suction sides.

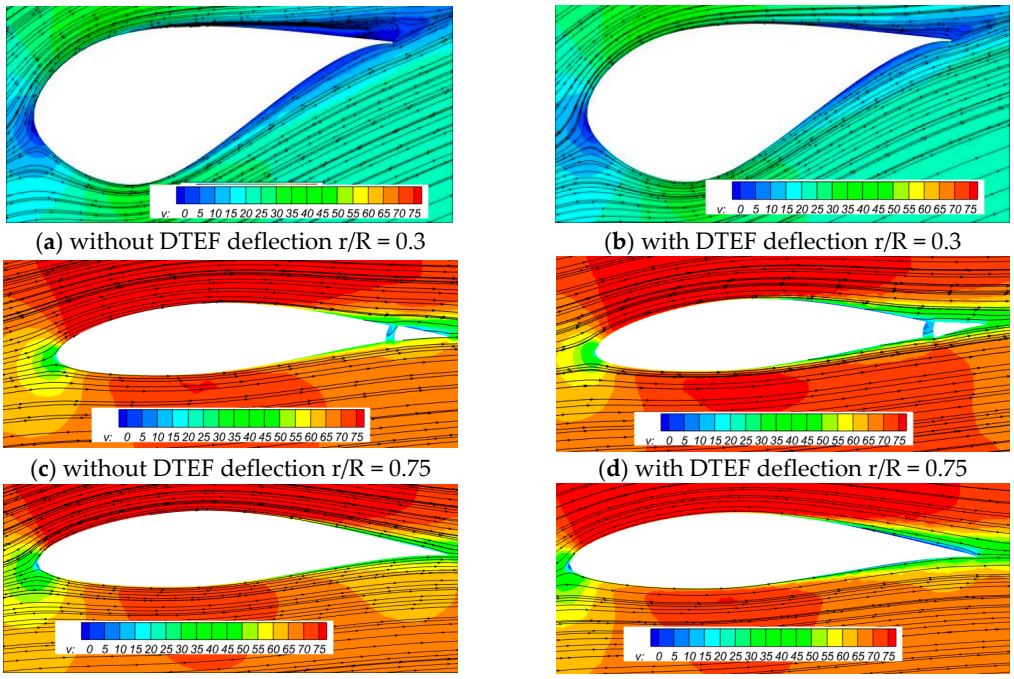

(**a**) without DTEF deflection r/R = 0.3 (**b**) with DTEF deflection r/R = 0.3

(**c**) without DTEF deflection r/R = 0.75 (**d**) with DTEF deflection r/R = 0.75

(**e**) without DTEF deflection r/R = 0.9 (**f**) with DTEF deflection r/R = 0.9

Figure 14. Contour maps of the velocity streamline distribution around the typical cross-section of the blade.

The deployment of the DTEF resulted in variations in flow structures around the blade. The vortical structures around the blade are identified using the Q criterion [17], and the vortical structures around the blade under the wind shear condition of 12 m/s of incoming wind were further analyzed. Specifically,

$$Q = -\frac{1}{2}(\|S\|^2 - \|\Omega\|^2) = -\frac{1}{2}\left[\left(\frac{\partial u}{\partial x}\right)^2 + \left(\frac{\partial v}{\partial y}\right)^2 + \left(\frac{\partial w}{\partial z}\right)^2\right] - \frac{\partial u}{\partial y}\frac{\partial v}{\partial x} - \frac{\partial u}{\partial z}\frac{\partial w}{\partial x} - \frac{\partial v}{\partial z}\frac{\partial w}{\partial y} \quad (9)$$

where S and Ω represent the strain and rotation tensors, respectively. A positive Q value indicates regions where the vorticity exceeds the strain rate.

Figure 15 illustrates the distribution of the vorticity iso-surface at $Q = 0.01$ around the blade at a wind speed of 12 m/s. Throughout the entire rotation cycle, the vortical structures around the rotor can be divided into three parts: the large-scale tip vortex that sheds from the blade tip, the root vortex that sheds from the cylindrical root of the blade, and the boundary vortex that separates from the suction surface of the blade at the mid-span. These three vortical flows each exhibited their own characteristics and influence ranges. The tip vortex featured a relatively large scale and high strength, and its root vortex was observed in the far-field downstream, demonstrating strong dynamic characteristics and significant far-field effects. This vortex, forming at the blade tip and spreading downstream due to high-speed rotation, may have a considerable impact on the surrounding environment and even adjacent blades.



(**a**) without DTEF deflection (**b**) with DTEF deflection

Figure 15. The contour surface plot of vorticity distribution around the blade (Q = 0.01).

In contrast, the boundary vortex that separates from the blade's suction surface is relatively weaker, and its formation is closely related to the flow separation on the blade surface. The deflection of the DTEF triggered significant changes in the shape and position of the original boundary vortex. Without flap deflection, flow separation at the trailing edge of the blade typically formed a relatively concentrated shedding vortex structure. However, this concentrated vortex structure was disrupted when the DTEF was deflected, accelerating the dissipation of the vortex structure. Additionally, flap deflection also stimulated the generation of new vortex structures.

The time-averaged vorticity distribution at several typical spanwise positions of the blade was extracted and analyzed to further investigate the changes in the vortical structures within the flow field caused by flap deflection, as displayed in Figure 16. These vorticity maps detail the specific distribution of vorticity, including the sizes, shapes, and relative positions of the vortices, providing a deeper understanding of the effect of flap deflection on the trailing-edge flow field.

Consistent with the overall vorticity distribution around the blade, the vorticity distribution maps at different cross-sectional positions demonstrate that the deflection of the DTEF alleviated the vortex-shedding phenomenon originally caused by flow separation. Meanwhile, flap deflection generated new vortex structures in the flow field at the trailing edge of the blade. A vortex dynamics analysis suggests that the generation and positional changes in these new vortices influenced the location of the flow separation point, as evidenced in Figure 14. This was because the new vortex structures provided additional energy input into the flow field and thus helped the airflow overcome viscous resistance while lowering the likelihood of flow separation. As a result, the flow separation around

the blade underwent significant changes, aligning with similar findings obtained in a study on synthetic jets conducted in 2022 [18].

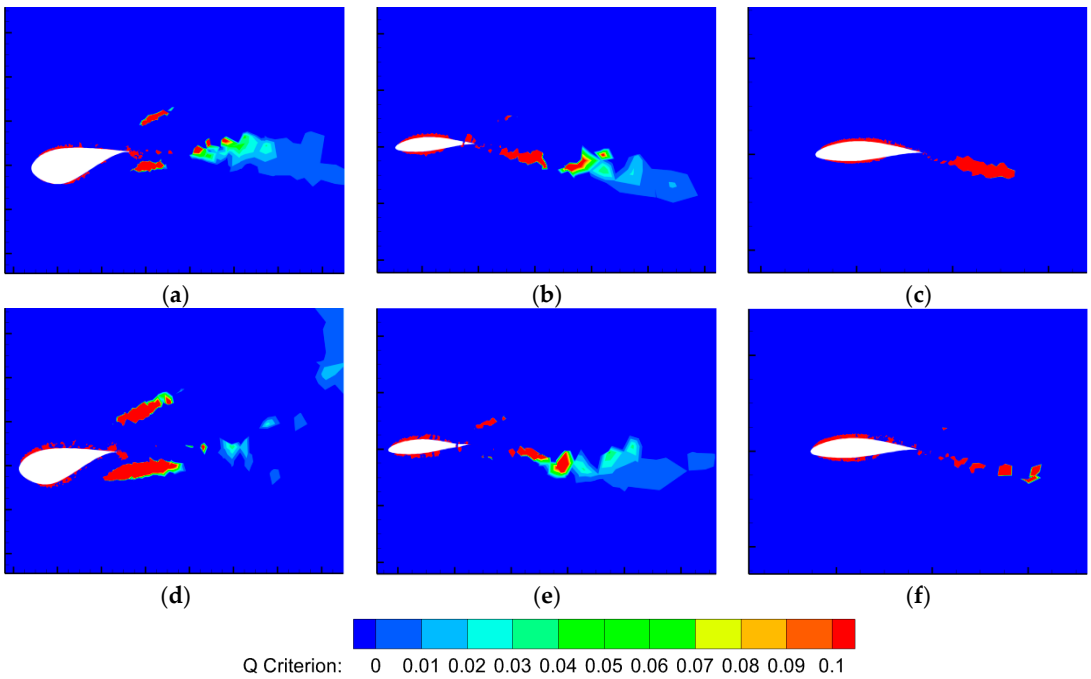

Figure 16. Vorticity distribution contour maps of the blade's cross-section. (**a**) r/R = 0.3 without DTEF deflection; (**b**) r/R = 0.75 without DTEF deflection; (**c**) r/R = 0.9 without DTEF deflection; (**d**) r/R = 0.3 with DTEF deflection; (**e**) r/R = 0.75 with DTEF deflection; (**f**) r/R = 0.9 with DTEF deflection.

Based on the aforementioned vorticity distribution results, vortex dynamics methods were employed to further describe the generation process and dynamic characteristics of the vortex system. Boundary vorticity flux (BVF) is a crucial theoretical concept used to represent the generation of vorticity and the diffusion process caused by viscosity within the boundary layer. Specifically, boundary vorticity flux quantifies the generation or intensification of vortices near the boundary. The positive boundary vorticity flux indicates the generation of vortices or their increasing intensity in the vicinity of the boundary. Conversely, a negative value signifies a reduction in the vortex intensity or vortex dissipation. The formula for calculating boundary vorticity flux is

$$\vec{\sigma} = \vec{\sigma_a} + \vec{\sigma_f} + \vec{\sigma_p} + \vec{\sigma_{vis}} = \vec{n} \times (\vec{a} - \vec{f} + \frac{1}{\rho}\nabla\overline{p}) + \nu(\vec{n} \times \nabla) \times \overline{\omega} \tag{10}$$

For the wind turbine conditions we simulated, $Re >> 1$, at which point σ_p dominates, and σ_p is the fundamental mechanism for vorticity generation. The deflection of the DTEF primarily affects the vortices in the x-direction. Therefore, the component of σ_p in the x-direction was extracted in this study, expressed as

$$\vec{\sigma_{px}} = \frac{\partial p}{\partial z}\vec{n_y} - \frac{\partial p}{\partial y}\vec{n_z} \tag{11}$$

As observed from the boundary vorticity flux distribution map (Figure 17), the range of positive boundary vorticity flux distribution increased in the region behind the trailing edge of the flap after the flap was applied. In other words, there was a trend of higher vorticity generation near the boundary at the location of the flap after the flap was applied, consistent with the earlier observation that the application of the DTEF contributed to the formation of new vortex structures in the flow field around the blade.

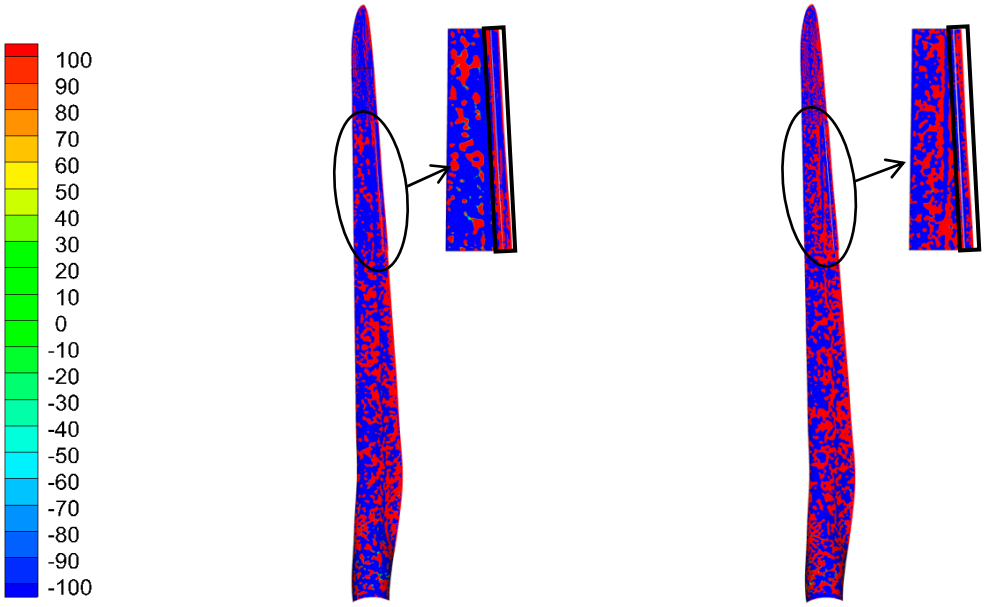

(**a**) without DTEF deflection (**b**) with DTEF deflection

Figure 17. Boundary vorticity flux distribution contour maps of the blade's surface.

In this study, the local flow field at the position where the flap interacts with the blade was extracted and analyzed in detail to investigate the reason why the DTEF had an influence on the overall flow characteristics around the blade.

Through a previous analysis of the tangential and normal force coefficients along the spanwise position of the blade, as well as the changes in the flow field around the entire blade surface under the influence of the DTEF, it can be concluded that the deflection of the DTEF affected not only the flow characteristics at the location of the flap but also the flow characteristics at other locations on the blade where no flap as installed. Figure 18 presents the local streamlines in the longitudinal cross-section at the contact point between the flap and the blade.

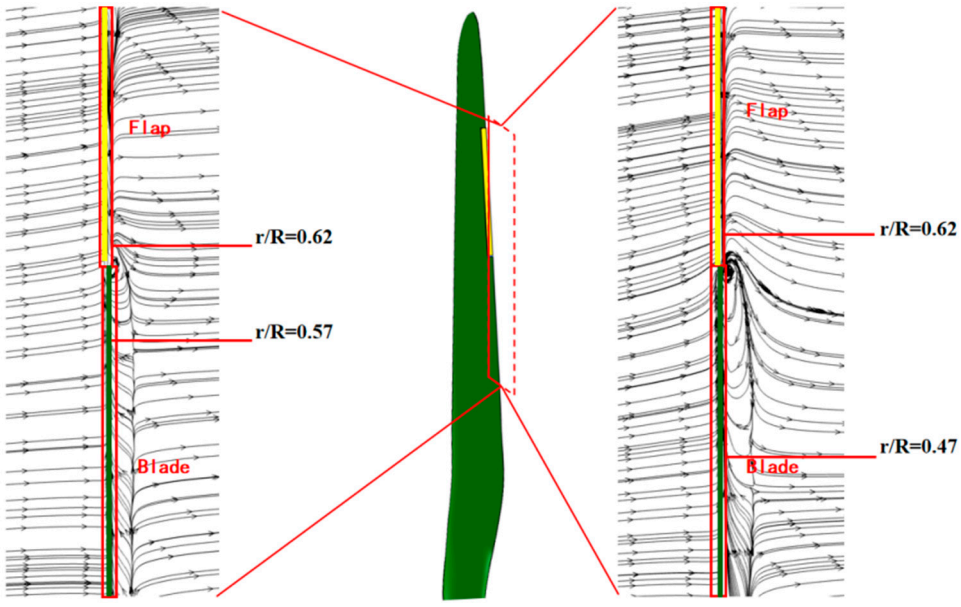

(**a**) (**b**)

Figure 18. Local streamline distribution of longitudinal section of blade: (**a**) without DTEF deflection; (**b**) with DTEF deflection.

As illustrated in Figure 18, the deflection of the DTEF reinforced the spanwise flow from the location of the flap toward the blade. For the baseline blade, the fluid exhibited spanwise flow only in the range of 57–62% of the blade span because of flow separation. However, after flap deflection, the flow separation at the flap location as weakened, and the spanwise flow region expanded to 47–62%.

After the modified flow structure characteristics were discussed, a schematic diagram of the change in flow characteristics around the blade was created to discuss the change between the baseline and the controlled situation, and to explain the effect of the changed flow structure on the pressure fluctuations, and thus to account for the fluctuating aerodynamic load on the blade.

Figure 19 illustrates the mechanism of the altered spanwise flow when the DTEF was implemented. The deflection of the DTEF altered the flow characteristics at the flap's location, generating a pressure difference between the flap and the blade, as supported by the blade surface pressure distribution in Figure 12. Influenced by this pressure difference, the fluid flowed to both sides of the flap's spanwise location. This affected the original flow around the blade at the flap's vicinity and hence the overall aerodynamic characteristics of the entire blade.

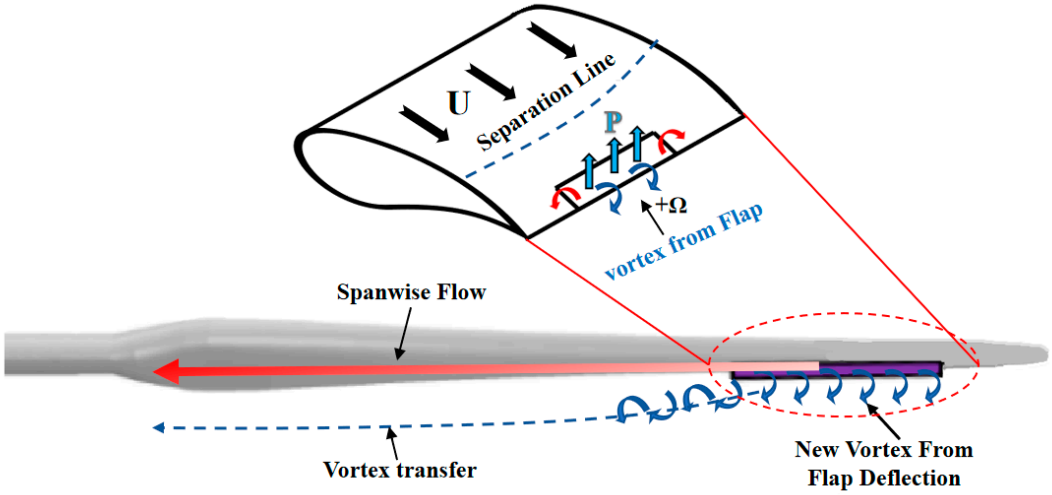

Figure 19. Schematic diagram of spanwise flow in blade flap position.

Simultaneously, the vortex structures moved in the direction of fluid development. This suggests that as the fluid flowed spanwise, the vortex structures generated by flap deflection also moved toward the blade root and blade tip. These vortex structures carried additional energy, which supplemented the energy at the location of the original flow separation on the blade, thus weakening the flow separation on the leeward side of the blade. Consequently, the pressure difference between the blade's windward and leeward sides decreased, bringing about thrust reduction and a load alleviation effect.

The analysis process described above, combined with the results from earlier sections, reveals the entire transmission process and mechanism analysis of how flap deflection affects the overall performance parameters of the blade. This further validates the accuracy of the computational results presented in Section 2.

5. Conclusions

The mechanism of aerodynamic load reduction of a large-scale wind turbine blade with trailing edge flaps was investigated in this study. Numerical calculations were performed on the "intelligent blade" simulation platform established in previous works of the research team. The application of the DTEF contributed to significant alterations in flow structures

around the blade and thus caused a substantial reduction in the blade root pitching moment by 12.4% compared to the baseline case. The conclusions are as follows:

(1) The deflection of the DTEF brought about a reduction of 20.58% in the average thrust exerted on the blade and a decrease of 13.20% in the standard deviation. The surface pressure distribution results imply that the pressure differences between the upper and lower surfaces were curtailed by 12%, 15%, and 8% for the areas at the 30%, 75%, and 90% spanwise sections of the blade, respectively. This indicates a decrease in the aerodynamic force exerted by the surrounding fluid on the blade surface. Consequently, the aeroelastic response of the blade was mitigated because of the weakened aerodynamic load.

(2) The oscillation of the DTEF disrupted the original vortex structures in the vicinity of the flap while generating new vortex structures. These newly formed vortices carried energy that compensated for the energy dissipation caused by flow separation at the original location on the blade. This suppressed flow separation on the leeward side of the blade, thereby influencing the pressure distribution in the surrounding flow field. Moreover, the altered flow structure facilitated partial regulation of the aerodynamic forces acting on the blade and lowered the thrust experienced by the blade.

(3) The deflection of the DTEF altered the flow characteristics at the location of the flap. The local pressure increased in the direction of the flap deflection, forming a pressure gradient between the DTEF and the blade. Driven by this pressure difference, the fluid flowed toward the flow direction of the flap along the spanwise direction. This influenced the original flow conditions around the blade and therefore the aerodynamic characteristics of the entire blade.

Author Contributions: Conceptualization, M.Z.; Methodology, B.Z.; Software, Y.L.; Validation, Y.L. and N.Z.; Formal analysis, M.Z.; Investigation, B.Z.; Data curation, H.J.; Writing—original draft, Y.L.; Writing—review & editing, Y.L.; Supervision, M.Z.; Project administration, M.Z. and Z.Z. All authors have read and agreed to the published version of the manuscript.

Funding: This work was supported by the National Key Research and Development Program of China (2022YFB4201200), the Key Projects of Stable Funding Support for Universities in Shenzhen (GXWD20220817140906007), and the Guangdong Basic and Applied Basic Research Foundation (2024B1515250004).

Data Availability Statement: The data that support the findings of this study are available from the corresponding author, upon reasonable request.

Conflicts of Interest: Author Zhaohuan Zhang was employed by the company State Grid Shandong Electric Power Company. The remaining authors declare that the research was conducted in the absence of any commercial or financial relationships that could be construed as a potential conflict of interest.

References

1. Lackner, M.A.; van Kuik, G. A comparison of smart rotor control approaches using trailing edge flaps and individual pitch control. *Wind Energy Int. J. Prog. Appl. Wind. Power Convers. Technol.* **2010**, *13*, 117–134. [CrossRef]
2. Cooperman, A.M.; Chow, R.; Van Dam, C.P. Active load control of a wind turbine airfoil using microtabs. *J. Aircr.* **2013**, *50*, 1150–1158. [CrossRef]
3. Daynes, S.; Weaver, P.M. Design and testing of a deformable wind turbine blade control surface. *Smart Mater. Struct.* **2012**, *21*, 105019. [CrossRef]
4. Andersen, P.B. Advanced Load Alleviation for Wind Turbines Using Adaptive Trailing Edge Flaps: Sensoring and Control. Ph.D. Thesis, Technical University of Denmark, Roskilde, Denmark, 2010.
5. Wei, X.; Ng, B.F.; Zhao, X. Aeroelastic load control of large and fexible wind turbines through mechanically driven flaps. *J. Frankl. Inst.* **2019**, *356*, 7810–7835. [CrossRef]

6. Perez-Becker, S.; Marten, D.; Paschereit, C.O. Active flap control with the trailing edge flap hinge moment as a sensor: Using it to estimatelocal blade inflow conditions and to reduce extreme blade loads and defections. *Wind. Energy Sci.* **2021**, *6*, 791–814. [CrossRef]
7. Wolff, T.; Seume, J. Airfoil with Morphing Trailing Edge for Load Reduction in Wind Turbines. In Proceedings of the 33rd Wind Energy Symposium, Kissimmee, FL, USA, 5–9 January 2015; p. 1662.
8. Wolff, T.; Ernst, B.; Seume, J.R. Aerodynamic behavior of an airfoil with morphing trailing edge for wind turbine applications. *J. Phys. Conf. Ser.* **2014**, *524*, 012018. [CrossRef]
9. Andersen, P.B.; Gaunaa, M.; Bak, C.; Buhl, T. Load alleviation on wind turbine blades using variable airfoilgeometry. In Proceedings of the EWEC, Athens, Greece, 27 February–2 March 2006.
10. Qian, Y.; Zhang, Y.; Sun, Y.; Wang, T. Numerical investigations of the flow control effect on a thick wind turbine airfoil using deformable trailing edge flaps. *Energy* **2023**, *265*, 126327. [CrossRef]
11. Zhang, M.; Yu, W.; Xu, J. Aerodynamic physics of smart load control for wind turbine due to extreme wind shear. *Renew. Energy* **2014**, *70*, 204–210. [CrossRef]
12. Zhang, M.; Tan, B.; Xu, J. Parameter study of sizing and placement of deformable trailing edge flap on blade fatigue load reduction. *Renew. Energy* **2015**, *77*, 217–226. [CrossRef]
13. Zhang, M.; Li, X.; Tong, J.; Xu, J. Load control of floating wind turbine on a Tension-Leg-Platform subject to extreme wind condition. *Renew. Energy* **2020**, *151*, 993–1007. [CrossRef]
14. Yang, H. Simulation and Experimental Study of Intelligent Control System for Trailing Edge Flap Load of Large Wind Turbine Blades. Ph.D. Thesis, University of Chinese Academy of Sciences (Institute of Engineering Thermophysics), Beijing, China, 2020.
15. Jonkman, J.; Butterfield, S.; Musial, W.; Scott, G. *Definition of a 5-MW Reference Wind Turbine for Offshore System Development*; (No. NREL/TP-500-38060); National Renewable Energy Lab. (NREL): Golden, CO, USA, 2009.
16. Anderson, J.D. *Fundamentals of Aerodynamics*; McGraw-Hil: New York, NY, USA, 1984.
17. Hunt, J.C.R.; Wang, Z.; Moin, P. Eddies and strain: The dynamic behavior of turbulent flows. *J. Fluid Mech.* **1988**, *140*, 381–414.
18. Zhang, Q. *Study on Flow Separation Characteristics of NACA0012 Airfoil and Flow Control of Synthetic Jet at Low Reynolds Number*; North University of China: Taiyuan, China, 2022.

Disclaimer/Publisher's Note: The statements, opinions and data contained in all publications are solely those of the individual author(s) and contributor(s) and not of MDPI and/or the editor(s). MDPI and/or the editor(s) disclaim responsibility for any injury to people or property resulting from any ideas, methods, instructions or products referred to in the content.